



Plasmonic Forward Scattering Effect in Organic Solar Cells: A Powerful Optical Engineering Method

Se-Woong Baek^{1,3}, Jonghyeon Noh^{1,3}, Chun-Ho Lee^{2,3}, BongSoo Kim⁴, Min-Kyo Seo^{2,3} & Jung-Yong Lee^{1,3}

¹Graduate School of Energy, Environment, Water, and Sustainability (EEWS), ²Department of Physics, ³KI for the NanoCentury, Korea Advanced Institute of Science and Technology (KAIST), Daejeon, 305-701, Republic of Korea, ⁴Photo-electronic Hybrids Research Center, Korea Institute of Science and Technology (KIST), Seoul, 136-791, Republic of Korea.

SUBJECT AREAS:
SOLAR ENERGY AND
PHOTOVOLTAIC
TECHNOLOGY
NANOPHOTONICS AND
PLASMONICS
NANOPARTICLES
MOLECULAR ELECTRONICS

Received
5 March 2013

Accepted
10 April 2013

Published
25 April 2013

Correspondence and
requests for materials
should be addressed to
J.-Y.L. (jungyong.lee@
kaist.ac.kr)

In this report, plasmonic effects in organic photovoltaic cells (OPVs) are systematically analyzed using size-controlled silver nanoparticles (AgNPs, diameter: 10 ~ 100 nm), which were incorporated into the anodic buffer layer, poly(3,4-ethylenedioxythiophene):poly(styrenesulfonate) (PEDOT:PSS). The optical properties of AgNPs tuned by size considerably influence the performance levels of devices. The power conversion efficiency (PCE) was increased from 6.4% to 7.6% in poly[N-9-hepta-decanyl-2,7-carbazole-alt-5,5-(4,7-di-2-thienyl)-2,1,3-benzothiadiazole] (PCDTBT):[6,6]-phenyl C₇₁-butyric acid methyl ester (PC₇₀BM) based-OPVs and from 7.9% to 8.6% in polythieno[3,4-b]thiophene/benzodithiophene (PTB7):PC₇₀BM based-OPVs upon embedding the AgNPs. The external quantum efficiency (EQE) was significantly enhanced by the absorption enhancement due to the plasmonic scattering effect. Finally, we verified the origin of the size-dependent plasmonic forwarding scattering effect of the AgNPs by visualizing the scattering field with near-field optical microscopy (NSOM) and through analytic optical simulations.

Organic photovoltaic (OPV) cells have much potential as next-generation solar cells because they are lightweight, flexible and can be produced inexpensively. Recently, the power conversion efficiency (PCE) of organic bulk heterojunction solar cells was reported to surpass 8 ~ 9%^{1,2}. However, the relatively low PCE of OPV cells compared with inorganic photovoltaic cells needs to be enhanced even more before these cells are commercially viable. Due to the low carrier mobility of the organic materials, the internal quantum efficiency (IQE) tends to decrease as the thickness of the active layer increases. For active layers with a thickness of ~ 100 nm in a bulk heterojunction system, it is difficult to absorb all of the incident photons. Owing to this ultrathin film thickness, the low light absorption tends to act as a bottleneck, preventing high efficiency in organic solar cells. Many researchers have tried to develop new polymer materials that have broad absorption spectra³, high carrier mobility⁴ and an appropriate optical band gap⁵ to achieve high PCE but the issue of insufficient absorption has yet to be completely overcome by conventional OPV cell structures. The use of optical engineering to enhance light absorption is inevitable in OPVs due to the trade-off relationship between the absorption capabilities and the IQE. Various approaches, including tandem structures^{2,6,7}, surface texturing⁸, metal nano-gratings⁹, resonance cavity¹⁰ and ray-optical light trapping systems¹¹⁻¹³ have been suggested to increase the optical absorption. Among these approaches, recently there has been growing interest in the use of metal nanoparticles (MNPs) in OPVs^{7,14-30} because the localized surface plasmon resonance (LSPR) effect of MNPs has the potential to boost the absorption of the active layer. In addition, the easy tunability of the optical properties by modifying size³¹, shape³² and surrounding materials³³ of MNPs has shown high potential as an optical engineering tool in thin-film optoelectronic devices. Many research groups have reported PCE enhancements by employing MNPs in what have been termed *plasmonic* OPVs. In addition, there have been many theories of the mechanism of PCE enhancement, such as the enhanced carrier effect and the exciton lifetime³⁴, conductivity¹⁵, and the surface morphology²³ as modified by incorporating MNPs. However, the exact roles of the LSPR effect in the OPVs are not well understood.

The LSPR effect of MNPs occurs by interaction between oscillating free electrons in the MNPs and incident light. The LSPR of MNPs have the MNPs not only scatter anisotropically, but also absorb the incident light. To investigate the scattering and absorption efficiency, simulations of an isolated AgNP in PEDOT:PSS were performed²⁰. Figure 1(a) shows the ratio of the scattering to the absorption power integrated from 300 to

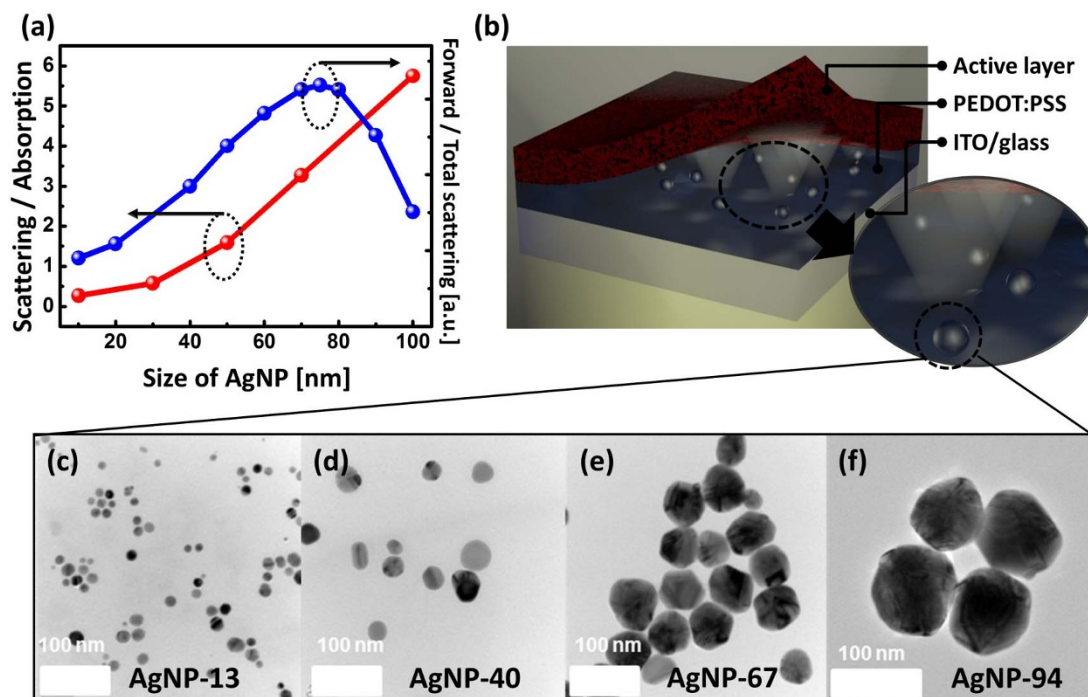


Figure 1 | Schematic of a plasmonic OPV and optical simulation results. (a) The analytical optical simulations were performed based on a previous report²⁰. Red: ratio of the total scattering power to the total absorption power value of various sizes of AgNPs. The power was integrated at wavelengths ranging from 300 nm to 800 nm. Blue: ratio of the forward scattering to the total scattering of a spherical AgNP in PEDOT:PSS. The sizes of the AgNPs used in the simulation were average sizes. (b) Schematic of a plasmonic OPV. The device structure is glass/ITO/PEDOT:PSS with a AgNPs/PCDTBT:PC₇₀BM (or PTB7:PC₇₀BM)/TiO_x/Al reflector. The inset schematic describes the plasmonic forward scattering effect of the AgNPs in the PEDOT:PSS layer. (c–f) TEM images of (c) AgNP-13, (d) AgNP-40, (e) AgNP-67 and (f) AgNP-94.

800 nm for nanoparticles of different sizes (red line). For PV applications, ideally, the ratio should be close to 1 because the power absorbed by the AgNP is dissipated as Joule heating. Although the absorption power of a small AgNP (<40 nm) dominates the scattering power, with a further increase in the size, the scattering power becomes stronger than the absorption power. Hence, it can be concluded that large MNPs (>40 nm) may be beneficial from an optical point of view. However, few demonstrations have been reported on the performance-dependence of PVs on the size of embedded MNPs in the devices.

In this report, we demonstrate organic photovoltaic cells with size-controlled AgNPs (10 ~ 100 nm) doped in an anodic buffer layer of poly(3,4-ethylenedioxythiophene):polystyrenesulfonate (PEDOT:PSS). We used AgNPs because AgNPs show superior scattering efficiency to any other MNPs, as demonstrated in Fig. S1. We study the plasmonic size effect of MNPs on the PCE of OPVs and reveal the underlying mechanisms of the interplay between the MNPs and the OPVs experimentally.

Results

Plasmonic design of organic solar cells. A schematic illustration of the proposed device structure is shown in Fig. 1(b). Anodic buffer layer consisting of PEDOT:PSS was doped with AgNPs of various sizes to induce forward scattering efficiently. The doping volume of the AgNP suspension was fixed at 40 vol% in order to maintain the thickness of the PEDOT:PSS at approximately 30 nm. The AgNP suspension was dispersed in deionized water so that it would be mixed well with the PEDOT:PSS solution. In this report, we fabricated two types of OPVs using poly[N-9-hepta-decanyl-2,7-carbazole-alt-5,5-(4,7-di-2-thienyl-2,1,3-benzothiadiazole)] (PCDTBT) and polythieno[3,4-b]thiophene/benzodithiophene (PTB7) as photoactive donors and [6,6]-phenyl C₇₁-butyric acid methyl ester (PC₇₀BM) as an acceptor. The control device structure was ITO/PEDOT:PSS/

Polymer:PC₇₀BM/TiO_x/Al. Our PCDTBT- and PTB7-based control devices have consistently shown PCEs of approximately 6.4% and 7.9%, respectively. It has been reported that PCDTBT:PC₇₀BM-based OPVs show as high PCE as 6%³⁵ or more with relatively low absorption and high IQE values³⁶. Therefore, appropriate optical engineering that can offset the low optical absorption without disturbing the high IQE will effectively improve the PCE.

Figures 1(c)–(f) show transmission electron microscopy (TEM) images of mono-dispersed AgNPs whose diameters range from 10 to 100 nm. We denoted the AgNPs having an average diameter of d nm as AgNP- d . A histogram of the exact size distribution is shown in Fig. S4 and the data are summarized in Table S1. Figure S3 shows that the scattering efficiency is influenced considerably by the size of the AgNPs, implying that the device performance can be also significantly affected by the size of the AgNPs.

Dependence of photovoltaic performance on AgNPs size. We investigated the plasmonic OPVs by modulating two conditions of the AgNPs: the size and the concentration. Figure 2(a) shows the representative current density (J)-voltage (V) characteristic of the best PCDTBT:PC₇₀BM-based OPV cells with AgNP-67 embedded in their PEDOT:PSS buffer layer at an optimal concentration of $4.5 \times 10^9/\text{cm}^2$ (red filled circles). The PCE was substantially improved from 6.4% to 7.6%, resulting mainly from the significant short circuit current (J_{sc}) enhancement of approximately 13%, from 11.22 mA/cm² to 12.67 mA/cm² (Table 1). The fill factor (FF) was slightly improved and the open circuit voltage (V_{oc}) was mostly unchanged, suggesting that the PCE enhancement resulted fundamentally from optical engineering via the incorporated AgNPs. Figure 2(b) compares the EQE, absorption and IQE of the best plasmonic OPV with those of a control OPV. The EQE and absorption were primarily enhanced at the wavelengths of 400 ~ 500 nm, precisely coinciding with the location of the LSPR of the AgNP-67, as revealed

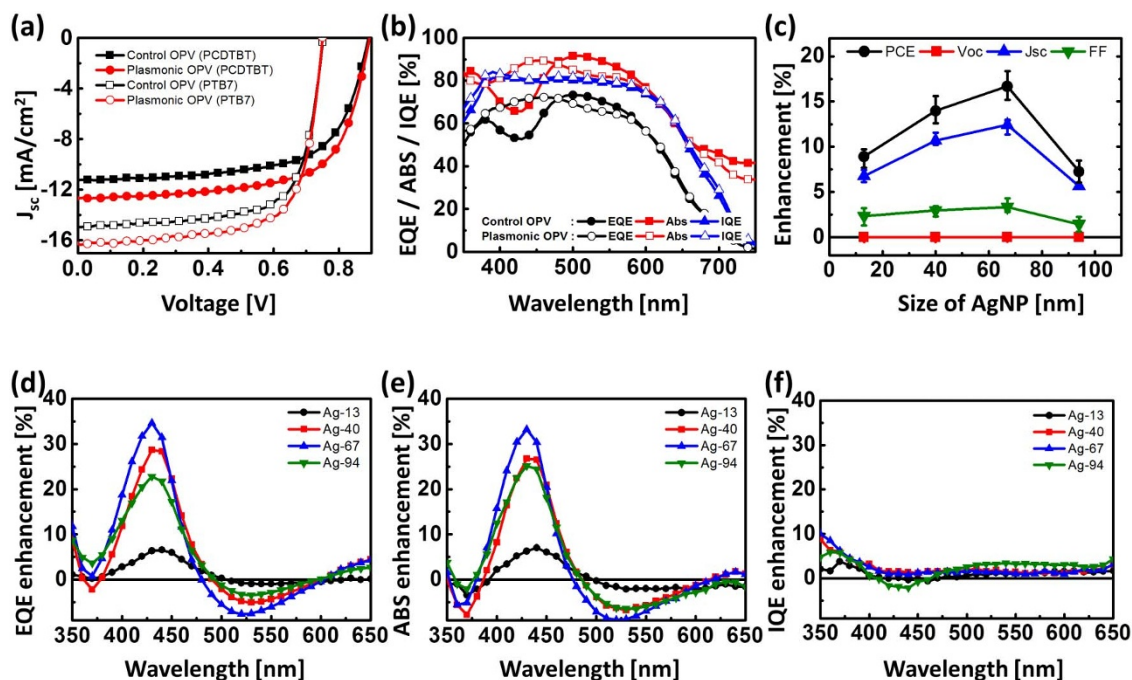


Figure 2 | *J-V* characteristics and spectral responses of plasmonic OPVs with various sizes of AgNPs. (a) The *J-V* curves of the best plasmonic OPV (red circles) and the control OPV (black squares). The filled and open symbols denote the PCDTBT:PC₇₀BM and PTB7:PC₇₀BM devices, respectively. The plasmonic devices were optimized in terms of their size and concentration. The optimum size and the concentration of the AgNPs were 67 nm and $4.5 \times 10^9/\text{cm}^2$, respectively. The best OPV achieved power conversion efficiency of 7.6% with PCDTBT:PC₇₀BM and 8.6% with PTB7:PC₇₀BM. (b) The EQE (black circles), absorption (red squares) and IQE (blue triangles) characteristics of a plasmonic OPV (open symbols) and a control device (filled symbols) of PCDTBT:PC₇₀BM, and (c) the maximum enhancement at various sizes of the AgNPs at the optimized concentrations. The *J_{sc}* and PCE values were significantly enhanced and optimized with AgNP-67. The error bars were acquired from at least 50 devices. (d) The EQE enhancement of OPVs with various sizes of AgNPs incorporated. (e) The absorption enhancement of OPVs incorporating various size-controlled AgNPs. (f) The IQE enhancement of OPVs with various sizes of AgNPs embedded: AgNP-13 (black circles), AgNP-40 (red squares), AgNP-67 (blue triangles (up)), and AgNP-94 (green triangles (down)).

in Fig. S2. Note that the relatively low absorption by the active materials in this region magnified the absorption enhancement effectively. For the PTB7:PC₇₀BM device (Fig. 2(a), open circles), the PCE was enhanced from 7.9% to 8.6% upon insertion of the AgNP-67 (Table 1). The *J_{sc}* value was essentially enhanced while the *V_{oc}* and *FF* remained unchanged, similar to PCDTBT:PC₇₀BM-based OPVs. The detailed EQE, absorption and IQE performance metrics are illustrated in Fig. S5. Figure S5(b) shows that the EQE and absorption were also greatly enhanced at the same spectral region, indicating that the PTB7:PC₇₀BM device and the PCDTBT:PC₇₀BM device were enhanced by the same mechanism.

Figure 2(c) and Table 1 show the size effects of the embedded AgNPs on the photovoltaic performances of the OPVs. For consistency of the results, at least 50 devices were fabricated at each condition. The complete statistical data of the devices performance are summarized in Table S2. For each AgNP size, the AgNPs were doped at optimal concentrations to yield the maximum PCE. The

maximum enhancement was gradually increased as the size of AgNPs was increased to 67 nm. Clearly, the enhancement of the PCE was dominantly determined by the enhancement of the *J_{sc}* value. The *FF* was slightly enhanced at all sizes of AgNPs, and the *V_{oc}* was not much affected. However, for AgNPs larger than 67 nm, the maximum enhancement declined.

Origin of AgNPs size effect. To investigate the origin of the size-dependent plasmonic effect on the PCE, the spectral responses of the OPVs were measured according to the size of AgNPs. Figure 2(d) illustrates that the external quantum efficiency (EQE) was primarily enhanced at wavelengths between 400 and 500 nm at all sizes and that the EQE enhancement peaked to 35% near the LSPR when AgNP-67 was embedded. However, when larger AgNPs (i.e., AgNP-94) were embedded in the OPVs, the EQE enhancement near the LSPR was reduced. In order to determine the influence of the AgNPs in more detail, we measured the spectral reflectance, $R(\lambda)$,

Table 1 | Characteristics of the plasmonic OPVs incorporating size-controlled AgNPs in the PEDOT:PSS layer. The table shows the optimized cell performance for each size

Polymer	AgNP	<i>V_{oc}</i> [V]	<i>J_{sc}</i> [mA/cm ²]	<i>FF</i> [%]	η [%]	<i>J_{sc}</i> (EQE) [mA/cm ²]
PCDTBT	Control device	0.89	11.22	0.64	6.4	11.20
	AgNP-13	0.89	11.98	0.66	7.0	11.63
	AgNP-40	0.89	12.42	0.66	7.3	12.10
	AgNP-67 (optimum)	0.89	12.67	0.67	7.6	12.30
	AgNP-94	0.89	11.87	0.66	6.9	12.01
PTB7	Control device	0.75	14.93	0.70	7.9	14.51
	AgNP-67 (optimum)	0.75	16.33	0.70	8.6	15.94



of the devices within an integrating sphere equipped with a photodetector; the total absorption of the entire device was estimated by $1 - R(\lambda)$. The measurements of both the EQE and the reflectance were performed simultaneously at the same spots with the same sample so as to obtain the most reliable results. Refer to the Methods for more details. Figure 2(e) illustrates the pattern of the absorption enhancement, which resembles that of the EQE, revealing that optical modulation by the AgNPs had a strong impact on the electrical performance of the OPVs. The partial reduction of EQE and absorption at the wavelength of from 500 ~ 550 nm is caused by the increased optical loss due to the reflection and relatively high absorption of the active materials. Reduction of the absorption at AgNP-94 resulted from the increased back reflection as compared to AgNP-67. However, it does not contradict our prediction that the stronger scattering by the larger AgNPs can effectively improve the PCE, as implied in Fig. 1(a); the total scattering was indeed enhanced, but the back scattering power dominated the forward fraction with an increase in the size of the AgNPs, as illustrated in Fig. S3. We calculated the IQE of the OPVs by dividing the EQE by the measured absorption, as depicted in Fig. 2(b). Fig. 2(f) illustrates the IQE enhancement. It should also be noted that our estimated IQE actually provides the *minimum* IQE of the OPVs because the estimated absorption consisted of the absorption by not only the active layer but also the MNPs and the electrodes. The IQE values were not greatly affected by the AgNPs at all sizes, except for AgNP-94, in which the IQE value near 400~450 nm showed a slight decrease, conceivably due to the absorption by the MNPs themselves. The unaffected IQE result strongly supports the fact that the enhanced J_{sc} resulted from the absorption enhancement from the plasmonic scattering by the AgNPs.

In fact, not only the scattering power but also the scattering direction must be considered, as the backward scattered power does not contribute to the absorption enhancement of the proposed OPVs. We calculated the amount of the forward scattering ratio to the total scattering power using optical simulations while assuming PEDOT:PSS as a medium and an incident wavelength of 430 nm, where the maximum EQE and absorption enhancement occurred, as shown in Figs. 2(d) and (e). Figure 1(a) (blue line) plots the result along with the size of the AgNPs; the forward scattering fraction is increased with an increase in size of the AgNP and is optimized at approximately 75 nm. Backward scattering grows stronger when the size of the AgNPs is greater than 75 nm while the total scattering power is

still enhanced. The angular scattering power distributions of AgNPs at various sizes are shown in Fig. S3. The experimental performances of the plasmonic OPVs in Fig. 2(c) agree well with the optical simulation results in Fig. 1(a) (blue line), providing solid evidence that the plasmonic *forward* light scattering effect by AgNPs greatly enhances the EQE and absorption of OPVs.

Visualization of plasmonic scattering by the AgNPs using near-field scanning optical microscopy (NSOM). Previous reports on plasmonic OPVs frequently analyzed the morphological variation of PEDOT:PSS upon the insertion of AgNPs^{23,25}. However, there have been few comprehensive reports on the optical properties of device films. Here, we visualized the degree of scattering of size-controlled AgNPs in a PEDOT:PSS layer using near-field scanning optical microscopy (NSOM) and verified the relationship between the scattering efficiency and the size of the AgNPs.

Samples of neat PEDOT:PSS and PEDOT:PSS with the AgNPs embedded were prepared and measured in the NSOM transmission mode. The samples were prepared at the optimal AgNP concentrations to give the maximum efficiency at each size. The scanning was performed using a laser diode (~ 20 mW) having a wavelength of 405 nm, close to the EQE and the absorption enhancement peak. The operating method is described in detail in the Methods. Figures 3(a–(d)), NSOM topography images reveal that most of the AgNPs were well dispersed without serious aggregation.

Figures 3(e)–(h) illustrate NSOM signal images which were attained by detecting the number of photons that were transmitted through the glass/ITO/AgNPs-doped PEDOT:PSS; the insets show the scattering profiles along the center line in each signal image. The absorption and the scattering characteristics of films can be analyzed from the signal images; the rough surface is attributed to the scattering of the incident light. Note that the partially dark spots are caused by light absorption by the AgNPs and PEDOT:PSS because such absorbed photons cannot be collected by a photodetector.

The signal roughness (i.e., degree of scattering) of a pristine PEDOT:PSS layer and PEDOT:PSS with AgNP-13, AgNP-67, and AgNP-94 exhibit root mean square (RMS) values of 0.36, 0.37, 0.87, and 0.64, respectively. The NSOM signal trend is also in good agreement with the analytic optical simulation results, as shown in Fig. 1(a) (blue line), also showing agreement with the plasmonic OPV performance results shown in Fig. 2(c). It is important to note that the scattering enhancement of 142% in the AgNP-67 case was

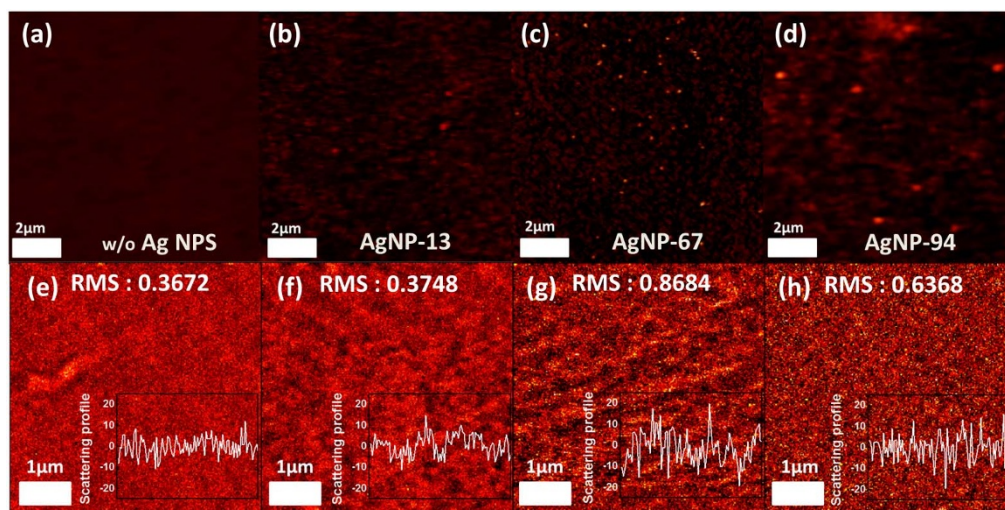


Figure 3 | Morphological and optical properties of AgNP-embedded PEDOT:PSS by NSOM. (a–d) NSOM topography images of a reference (neat PEDOT:PSS), PEDOT:PSS with AgNP-28, AgNP-67, and AgNP-94 embedded samples, respectively. (e–h) NSOM signal images excited by a laser diode (405 nm); the insets here show the scattering profiles across the center lines of the NSOM signal images. The optimized concentrations of the AgNPs were used at each size. The NSOM scan size was $5 \mu\text{m} \times 5 \mu\text{m}$.

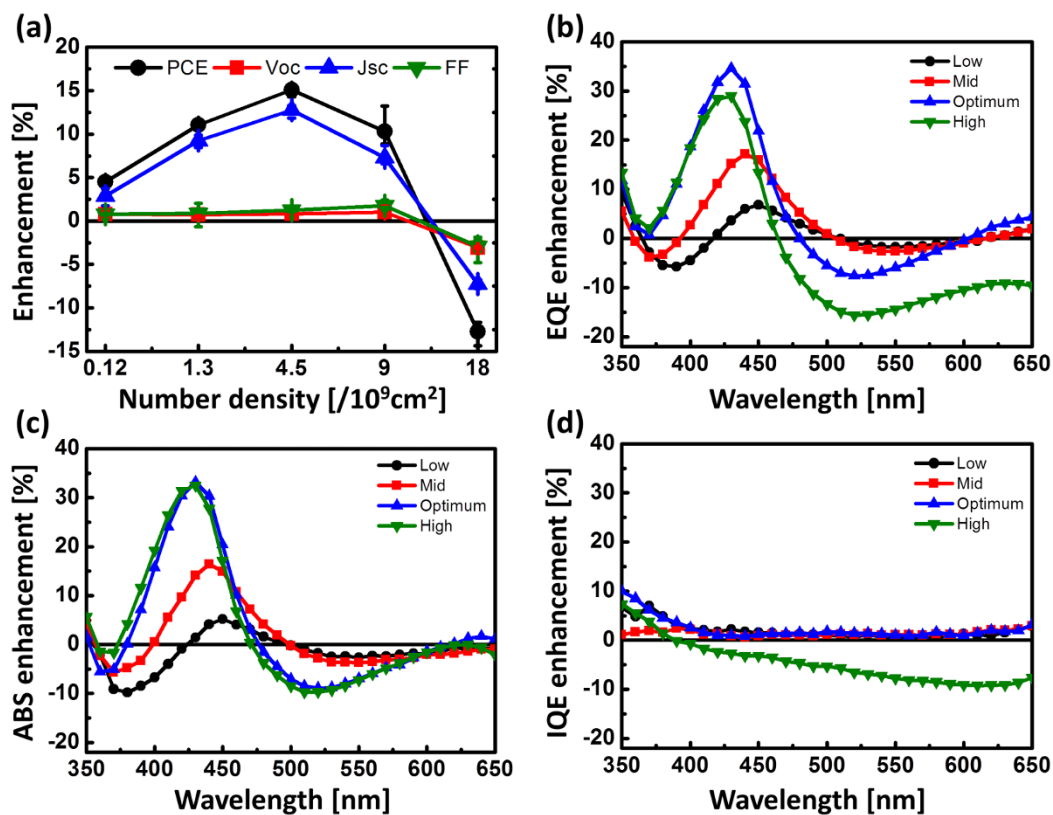


Figure 4 | Devices characteristics and spectral responses of plasmonic OPVs at various concentrations of AgNPs. (a) The PCE (black circles), J_{sc} (blue triangles (up)), V_{oc} (red squares), and FF (green triangles (down)) enhancements of the OPVs with AgNP-67 embedded at various concentrations, (b) the EQE enhancement at various concentrations, (c) the absorption enhancement at various concentrations, and (d) the IQE enhancement at various concentrations; low ($1.2 \times 10^9/\text{cm}^2$); medium ($1.3 \times 10^9/\text{cm}^2$); optimum ($4.5 \times 10^9/\text{cm}^2$); and high ($9.0 \times 10^9/\text{cm}^2$). The EQEs were enhanced primarily by the absorption enhancement, which was concentrated near the LSPR region (400–500 nm).

significantly larger than the topographical RMS enhancement of $\sim 40\%$, implying that the enhanced scattering resulted predominantly from the intrinsic scattering power by the AgNPs themselves, as explained above, rather than from the geometrical scattering effect caused by the rough surface.

Dependence of photovoltaic performance on AgNPs concentration. Next, we investigated the performance dependence of the plasmonic OPVs on the AgNP concentration, which needs to be chosen appropriately for the optimization of the devices. Figure 4(a) shows the performances enhancement of the OPVs with AgNP-67 embedded at various doping concentrations. The J_{sc} and PCE values were enhanced in proportion to the particle concentration and were optimized at a concentration of $4.5 \times 10^9/\text{cm}^2$. However, when the AgNP concentration was higher than the optimal value, both the J_{sc} and FF values were degraded. The V_{oc} value decreased slightly as well, as shown in Fig. 4(a). In particular, J_{sc} showed a noticeable decrease with an increase in the concentration of the AgNPs, essentially contributing to the reduced PCE. To understand the concentration dependence of the PCE enhancement, we investigated the EQE and total absorption of the plasmonic OPVs at various concentrations, as shown in Figs. 4(b)–4(d).

Figure 4(b) shows that the EQE was proportionally enhanced near the LSPR wavelength until the concentration reached the optimum value. In addition, the absorption enhancement follows the EQE tendency, as shown in Fig. 4(c). The IQE enhancement is nearly constant at all wavelengths, except for the “high” concentration, as shown in Fig. 4(d), providing further verification that the EQE is enhanced by the optical absorption enhancement. Note that with the

increase in the density, the peak position is blue-shifted due to the increased dipolar coupling between the MNPs³⁷, as indicated in Figs. 4(b) and (c). However, when the concentration of the AgNPs was higher than the optimum concentration, the EQE was degraded throughout nearly all of the wavelength range, especially at a longer wavelength, while the absorption enhancement was virtually identical to that at the optimal concentration, as shown in Figs. 4(b) and (c). As a result, the IQE was largely reduced in all wavelength ranges. Large clusters of AgNPs were formed during the deposition of PEDOT:PSS at a high concentration of AgNPs. Figure 4(c) reveals that the peak position was not shifted at a “high” concentration, thereby showing that the inter-particle distance was not reduced further by the increased density of the AgNPs from the “optimum” concentration³⁷. Figure S8(a) reveals that the AgNPs were well dispersed at the optimal concentration. However, as the concentration increased further, partially aggregated AgNPs were indeed observed, as illustrated in Fig. S8(b). At a “high” doping concentration of $9.0 \times 10^9/\text{cm}^2$, the actual total number density of approx. $5.5 \times 10^9/\text{cm}^2$, including large clusters, was slightly higher than the optimized concentration of approx. $4.5 \times 10^9/\text{cm}^2$ due to aggregation despite the fact that the doping concentration had doubled. Approximately 5% of the AgNPs were large clusters that had formed from smaller AgNPs, as shown in Fig. S8(b). The inset of Fig. S8(b) shows a cross-sectional scanning electron microscopy (SEM) image of aggregated Ag clusters in a PEDOT:PSS layer. The large AgNP cluster may have reduced the contact area between the PEDOT:PSS and the active layer, PCDTBT:PC₇₀BM, considerably reducing the FF value. The V_{oc} value was not affected in the “low” to “optimum” concentration range, but it showed a slight decrease at a higher



concentration. It is likely that the V_{oc} drop was caused by the exposure of Ag clusters on the PEDOT:PSS surface²⁷, increasing the number of short paths for charged carriers.

Discussion

We demonstrate highly efficient plasmonic OPVs that incorporate AgNPs into the anodic PEDOT:PSS layer. The PCE was enhanced to 7.6% by incorporating AgNPs 67 nm in size in a PCDTBT-based OPV, mainly because J_{sc} was significantly improved by approximately 13%. In addition, a PCE of 8.6% was achieved in PTB7-based OPVs after embedding the AgNPs. The EQE was remarkably enhanced near the LSPR wavelength of the AgNPs, and the improvement was primarily caused by the enhancement of the absorption capability. Unchanged conductivity of the PEDOT:PSS films by embedding the AgNPs (Fig. S9) proves also that the J_{sc} was enhanced primarily by an optical effect. The NSOM scattering signals strongly support that the scattering efficiency tuned by the size of the AgNPs influenced the device performance. We confirmed the plasmonic forward scattering effects from the NSOM measurements and in analytic optical simulations. This study demonstrates the possibility of manipulating the plasmonic optical properties of MNPs as a powerful optical engineering tool in OPVs.

Methods

Size-controlled AgNPs fabrication. We synthesized various size-controlled silver nanoparticles (AgNPs) by a polyol method^{38–41} and a borohydride reduction method⁴². For AgNPs 10 nm in size, 22.54 mg of silver perchlorate (AgClO_4) was dissolved in 100 ml of 3-type Milli-Q water and was stored in a refrigerator. 3.783 mg of sodium borohydride (NaBH_4) and 8.823 mg of sodium citrate (Na-cit) were added to 100 ml of the cold ice water bath under vigorous stirring. The solution became bright yellow immediately when 1 ml of the stock solution was added. For AgNPs 30 nm in size, 1.5 g of PVP (polyvinylpyrrolidone, Mw: 10,000) was dissolved in 75 ml of ethylene glycol. 1/37.5 wt% of silver nitrate (AgNO_3) was added after the PVP was dissolved completely and the solution was heated to 120°C at a rate of 1°C/min. AgNPs 50 nm in size were obtained with 1/25 wt% of silver nitrate (AgNO_3), and the solution was heated to 120°C at 5°C/min. The reactions were maintained for 1 hr and the samples were then cooled to room temperature. AgNPs of 70 nm and 100 nm could be obtained by changing only the mixing ratio of the PVP to AgNO_3 . The ratios were 8:1 (70 nm) and 6:1 (100 nm) in 20 ml of ethylene glycol. The solution was completely dissolved at room temperature and 2 ml of ammonia was added to the solution in a dropwise manner. The reactions were maintained for 4 hrs at 160°C under vigorous stirring. After cooling to room temperature, all solutions were washed in acetone and ethanol at least three times and stored in a refrigerator under a dark condition.

TiO_x solution preparation. Titanium(IV) isopropoxide ($\text{Ti}[\text{OCH}(\text{CH}_3)_2]_4$, 5 ml), 2-methoxyethanol ($\text{CH}_3\text{OCH}_2\text{CH}_2\text{OH}$, 20ml) and ethanolamine ($\text{H}_2\text{NCH}_2\text{CH}_2\text{OH}$, 2ml) were added to a three-necked flask in a nitrogen atmosphere. The solution was then stirred for 1 hr at room temperature, followed by heating at 80°C for 1 hr and 120°C for 1 hr. The solution was then cooled to room temperature and 10 ml of isopropanol (IPA) was added.

Device fabrication. The devices were fabricated on ITO-coated glass substrates with a sheet resistance of 22 Ω/sq . The glass/ITO substrates were pre-cleaned with acetone for 5 min and isopropyl alcohol (IPA) for 15 min and were dried in a vacuum oven overnight. After the substrates underwent a UV-ozone treatment, PEDOT:PSS (Al4083, Clevios) layers with and without size-controlled AgNPs (40 vol%) were spun onto the substrates at 3000 rpm for 30 s and were then annealed at 140°C for 10 min. The thickness of the PEDOT:PSS layer was approximately 30 nm. The PCDTBT:PC₇₀BM (1-materials : nano-c) at a weight ratio of 1 : 4 in a 1,2-dichlorobenzene(O-DCB) solution was completely dissolved for 24 hrs and then spun at 1100 rpm for 1 min on both PEDOT:PSS layers, after which the samples were dried at 70°C for 15 min. The PTB7:PC₇₀BM (1-materials : nano-c) at a weight ratio of 1 : 1.5 was dissolved in a chlorobenzene/1,8-dioctane (97% to 3%) solution and was spun at 2000 rpm for 35 s. The TiO_x 1 : 200 solution dissolved in methanol was spun at 3000 rpm and annealed at 80°C in air. Lastly, 100 nm of Al was deposited through a shadow mask by thermal evaporation on the devices. The active device area was measured with a microscope, showing a value of ~15 mm².

Characterization. Current density-voltage (J - V) curves were measured by a solar simulator (PEC-L12, Pecell Technologies) under 100 mW/cm² from a 150 W Xe short arc lamp filtered by an air mass 1.5 G filter. The external quantum efficiency (EQE) was measured by a spectral measurement system (K3100 IQX, McScience Inc.). The light source (a xenon arc lamp at 300 W) was used with a monochromator (Newport) and an optical chopper (MC 2000 Thorlabs). The spectral absorption by the devices was directly measured at the system immediately after the measurement of

the EQE. The measurement setup for the absorption measurement was as follows: the incident monochromatic light is absorbed in the device area through an integration sphere. The device is tilted at about 8° because the reflected light must be scattered inside the integration sphere. Therefore, the reflected light is scattered in the integration sphere and collected by a photodetector located in the integration sphere. The device absorption was calculated by $1 - R(\lambda)$, where $R(\lambda)$ denotes the wavelength-dependent reflectance data. Finally, the internal quantum efficiency (IQE) was determined by dividing the EQE by the absorption. The extinction spectra were measured by UV-vis-NIR spectrophotometers (UV-3600, Shimadzu). To visualize the AgNPs, field emission scanning electron microscopy (FE-SEM, FEI Sirion) and field emission transmission electron microscope (FE-TEM, FEI Tecnai G² f30 S-Twin, 300 KeV) were used to investigate the cross-section of the devices and the dimension of the AgNPs.

Near-field scanning optical microscopy. A scanning near-field optical microscope (Alpha300S, WiTec) was used to measure the NSOM topography and NSOM signal (i.e., scattering profile). A silicon cantilever with a hollow aluminum pyramid as a tip was used to measure the topography. The detailed NSOM measurement process is as follows. As soon as the NSOM tip approached to the sample surface closely, the samples were excited by a laser diode (wavelength: 405 nm) that was well matched with absorption enhancement region. The NSOM tip captured the evanescent wave while scanning the samples above the PEDOT:PSS surface and the signals were collected and converted to the profile images. The tip aperture size was 60 nm. The scattering profiles (Figs. 3(e)–3(h) insets) were surface line graphs of the NSOM signal images (Figs. 3(e)–3(h)). The topography images were scanned in an area of 10 $\mu\text{m} \times 10 \mu\text{m}$ and the NSOM signals were scanned in an area of 5 $\mu\text{m} \times 5 \mu\text{m}$. The scanning rate was 1 sec/line.

1. He, Z. C. *et al.* Enhanced power-conversion efficiency in polymer solar cells using an inverted device structure. *Nature Photonics* **6**, 591–595 (2012).
2. Dou, L. T. *et al.* Tandem polymer solar cells featuring a spectrally matched low-bandgap polymer. *Nature Photonics* **6**, 180–185 (2012).
3. Soci, C. *et al.* Photoconductivity of a low-bandgap conjugated polymer. *Advanced Functional Materials* **17**, 632–636 (2007).
4. Sun, Y. M. *et al.* Solution-processed small-molecule solar cells with 6.7% efficiency. *Nature Materials* **11**, 44–48 (2012).
5. Liang, Y. Y. *et al.* For the Bright Future-Bulk Heterojunction Polymer Solar Cells with Power Conversion Efficiency of 7.4%. *Advanced Materials* **22**, E135–+ (2010).
6. Kim, J. Y. *et al.* Efficient tandem polymer solar cells fabricated by all-solution processing. *Science* **317**, 222–225 (2007).
7. Yang, J. *et al.* Plasmonic Polymer Tandem Solar Cell. *ACS Nano* **5**, 6210–6217 (2011).
8. Campbell, P. & Green, M. A. Light Trapping Properties of Pyramidally Textured Surfaces. *Journal of Applied Physics* **62**, 243–249 (1987).
9. Yu, Z. F., Raman, A. & Fan, S. H. Fundamental limit of nanophotonic light trapping in solar cells. *Proceedings of the National Academy of Sciences of the United States of America* **107**, 17491–17496 (2010).
10. Sergeant, N. P. *et al.* Design of Transparent Anodes for Resonant Cavity Enhanced Light Harvesting in Organic Solar Cells. *Advanced Materials* **24**, 728–+ (2012).
11. Tvingstedt, K., Dal Zilio, S., Inngan, O. & Tormen, M. Trapping light with micro lenses in thin film organic photovoltaic cells. *Optics Express* **16**, 21608–21615 (2008).
12. Andersson, B. V., Wuerfel, U. & Inngan, O. Full day modelling of V-shaped organic solar cell. *Solar Energy* **85**, 1257–1263 (2011).
13. Peumans, P., Yakimov, A. & Forrest, S. R. Small molecular weight organic thin-film photodetectors and solar cells. *Journal of Applied Physics* **93**, 3693–3723 (2003).
14. Schaadt, D. M., Feng, B. & Yu, E. T. Enhanced semiconductor optical absorption via surface plasmon excitation in metal nanoparticles. *Applied Physics Letters* **86** (2005).
15. Wu, J. L. *et al.* Surface Plasmonic Effects of Metallic Nanoparticles on the Performance of Polymer Bulk Heterojunction Solar Cells. *ACS Nano* **5**, 959–967 (2011).
16. Pegg, L. J., Schumann, S. & Hattori, R. A. Enhancing the Open-Circuit Voltage of Molecular Photovoltaics Using Oxidized Au Nanocrystals. *ACS Nano* **4**, 5671–5678 (2010).
17. Ferry, V. E., Munday, J. N. & Atwater, H. A. Design Considerations for Plasmonic Photovoltaics. *Advanced Materials* **22**, 4794–4808 (2010).
18. Kulkarni, A. P., Noone, K. M., Munchika, K., Guyer, S. R. & Ginger, D. S. Plasmon-Enhanced Charge Carrier Generation in Organic Photovoltaic Films Using Silver Nanoprisms. *Nano Letters* **10**, 1501–1505 (2010).
19. Atwater, H. A. & Polman, A. Plasmonics for improved photovoltaic devices. *Nature Materials* **9**, 205–213 (2010).
20. Lee, J. Y. & Peumans, P. The origin of enhanced optical absorption in solar cells with metal nanoparticles embedded in the active layer. *Optics Express* **18**, 10078–10087 (2010).
21. Sha, W. E. I., Choy, W. C. H., Liu, Y. G. & Chew, W. C. Near-field multiple scattering effects of plasmonic nanospheres embedded into thin-film organic solar cells. *Applied Physics Letters* **99** (2011).



22. Zhu, J. F. *et al.* Plasmonic effects for light concentration in organic photovoltaic thin films induced by hexagonal periodic metallic nanospheres. *Applied Physics Letters* **98** (2011).
23. Fung, D. D. S. *et al.* Optical and electrical properties of efficiency enhanced polymer solar cells with Au nanoparticles in a PEDOT-PSS layer. *Journal of Materials Chemistry* **21**, 16349–16356 (2011).
24. Qu, D., Liu, F., Huang, Y. D., Xie, W. L. & Xu, Q. Mechanism of optical absorption enhancement in thin film organic solar cells with plasmonic metal nanoparticles. *Optics Express* **19**, 24795–24803 (2011).
25. Chen, H. C. *et al.* Large AuAg Alloy Nanoparticles Synthesized in Organic Media Using a One-Pot Reaction: Their Applications for High-Performance Bulk Heterojunction Solar Cells. *Advanced Functional Materials* **22**, 3975–3984 (2012).
26. Li, X. H. *et al.* Dual Plasmonic Nanostructures for High Performance Inverted Organic Solar Cells. *Advanced Materials* **24**, 3046–3052 (2012).
27. Xue, M. *et al.* Charge-carrier dynamics in hybrid plasmonic organic solar cells with Ag nanoparticles. *Applied Physics Letters* **98** (2011).
28. Kim, I., Lee, T. S., Jeong, D. S., Lee, W. S. & Lee, K. S. Size effects of metal nanoparticles embedded in a buffer layer of organic photovoltaics on plasmonic absorption enhancement. *Journal of Physics D-Applied Physics* **45** (2012).
29. Green, M. A. & Pillai, S. Harnessing plasmonics for solar cells. *Nature Photonics* **6**, 130–132 (2012).
30. Chen, X. *et al.* Broadband Enhancement in Thin-Film Amorphous Silicon Solar Cells Enabled by Nucleated Silver Nanoparticles. *Nano Letters* **12**, 2187–2192 (2012).
31. Lu, X. M., Rycenga, M., Skrabalak, S. E., Wiley, B. & Xia, Y. N. Chemical Synthesis of Novel Plasmonic Nanoparticles. *Annual Review of Physical Chemistry* **60**, 167–192 (2009).
32. Kelly, K. L., Coronado, E., Zhao, L. L. & Schatz, G. C. The optical properties of metal nanoparticles: The influence of size, shape, and dielectric environment. *Journal of Physical Chemistry B* **107**, 668–677 (2003).
33. Hutter, E. & Fendler, J. H. Exploitation of localized surface plasmon resonance. *Advanced Materials* **16**, 1685–1706 (2004).
34. Chen, F. C. *et al.* Plasmonic-enhanced polymer photovoltaic devices incorporating solution-processable metal nanoparticles. *Applied Physics Letters* **95** (2009).
35. Moon, J. S., Jo, J. & Heeger, A. J. Nanomorphology of PCDTBT:PC70BM Bulk Heterojunction Solar Cells. *Advanced Energy Materials* **2**, 304–308 (2012).
36. Park, S. H. *et al.* Bulk heterojunction solar cells with internal quantum efficiency approaching 100%. *Nature Photonics* **3**, 297–U295 (2009).
37. Zhao, L. L., Kelly, K. L. & Schatz, G. C. The extinction spectra of silver nanoparticle arrays: Influence of array structure on plasmon resonance wavelength and width. *Journal of Physical Chemistry B* **107**, 7343–7350 (2003).
38. Silvert, P. Y., Herrera-Urbina, R., Duvauchelle, N., Vijaykrishnan, V. & Elhsissen, K. T. Preparation of colloidal silver dispersions by the polyol process. I. Synthesis and characterization. *Journal of Materials Chemistry* **6**, 573–577 (1996).
39. Silvert, P. Y., Herrera-Urbina, R. & Tekaia-Elhsissen, K. Preparation of colloidal silver dispersions by the polyol process. 2. Mechanism of particle formation. *Journal of Materials Chemistry* **7**, 293–299 (1997).
40. Kim, D., Jeong, S. & Moon, J. Synthesis of silver nanoparticles using the polyol process and the influence of precursor injection. *Nanotechnology* **17**, 4019–4024 (2006).
41. Zhao, T. *et al.* Size-controlled preparation of silver nanoparticles by a modified polyol method. *Colloids and Surfaces a-Physicochemical and Engineering Aspects* **366**, 197–202 (2010).
42. Ung, T., Liz-Marzan, L. M. & Mulvaney, P. Controlled method for silica coating of silver colloids. Influence of coating on the rate of chemical reactions. *Langmuir* **14**, 3740–3748 (1998).

Acknowledgments

We sincerely appreciate the financial support of the Basic Science Research Program through the National Research Foundation of Korea (NRF) funded by the Ministry of Education, Science and Technology (MEST) (2012-0003991). We also gratefully acknowledge support from the Center for Inorganic Photovoltaic Materials (2012-0001172) through a grant funded by the MEST, Grant No. EEWS-2012-N01120012 from the EEWS Research Project of the office of the KAIST EEWS Initiative, KAIST Institute for the NanoCentury, and Samsung Display.

Author contributions

S.B. and J.L. conceived and designed the experiments and prepared the manuscript. S.B. synthesized the metal nanoparticles, fabricated the solar cells, and performed the optical simulations. S.B., J.N. and B.K. fabricated the solar cells and performed measurements such as the EQE and absorption. C.L. and M.S. designed and performed the NSOM experiments. All authors discussed the results and commented on the manuscript.

Additional information

Supplementary information accompanies this paper at <http://www.nature.com/scientificreports>

Competing financial interests: The authors declare no competing financial interests.

License: This work is licensed under a Creative Commons Attribution-NonCommercial-NoDerivs 3.0 Unported License. To view a copy of this license, visit <http://creativecommons.org/licenses/by-nc-nd/3.0/>

How to cite this article: Baek, S. *et al.* Plasmonic Forward Scattering Effect in Organic Solar Cells: A Powerful Optical Engineering Method. *Sci. Rep.* **3**, 1726; DOI:10.1038/srep01726 (2013).